# The role of an intense jet in the Tsugaru Strait in the formation of the outflow gyre revealed using high-frequency radar data

Hitoshi Kaneko[1,1], Ken'ichi Sasaki[1,1], Hiroto Abe[2,2], Shuichi Watanabe[1,1], and Yoshiaki Sato[1,1]

[1]Mutsu Institute for Oceanography
[2]Faculty of Fisheries Sciences

November 30, 2022

## Abstract

The seasonal pattern of the eastward jet through the Tsugaru Strait between 2014 and 2019 was investigated using surface velocity data obtained from high-frequency radar located in the eastern part of the strait. The vorticity-front-model was used to estimate the volume transport of low-vorticity water and the intensity of the vorticity gap at the front using the climatological mean zonal velocity distribution. The flow mode at the outlet was then defined as either the summer/autumn "gyre mode" or winter/spring "coastal mode". The distribution of the parameters was consistent with the theoretical understanding, showing that in addition to the volume transport, an increase in the vorticity gap can also contribute to the development of the gyre. The results also suggest an impact from the jet in the strait on the coastal flow along the coast of Japan.

# The role of an intense jet in the Tsugaru Strait in the formation of the outflow gyre revealed using high-frequency radar data

**H. Kaneko[1], K. Sasaki[1], H. Abe[1,2], S. Watanabe[1], and Y. Sato[1]**

[1] Mutsu Institute for Oceanography, Research Institute for Global Change, Japan Agency for Marine-Earth Science and Technology, Mutsu, Japan.

[2] Faculty of Fisheries Sciences, Hokkaido University, Hakodate, Japan.

Corresponding author: Hitoshi Kaneko (h_kaneko@jamstec.go.jp)

**Key Points:**

- Observational verification of the seasonal flow pattern theory of the Tsugaru Warm Current based on velocity data from high-frequency radar

- Importance of vorticity gap at the front of the jet recognized in addition to the volume transport of the current on the flow pattern change

- Effectiveness of high-frequency radar with diagnostic scheme improves understanding of the role of the strait in coastal flow around Japan

**Abstract**

The seasonal pattern of the eastward jet through the Tsugaru Strait between 2014 and 2019 was investigated using surface velocity data obtained from high-frequency radar located in the eastern part of the strait. The vorticity-front-model was used to estimate the volume transport of low-vorticity water and the intensity of the vorticity gap at the front using the climatological mean zonal velocity distribution. The flow mode at the outlet was then defined as either the summer/autumn "gyre mode" or winter/spring "coastal mode". The distribution of the parameters was consistent with the theoretical understanding, showing that in addition to the volume transport, an increase in the vorticity gap can also contribute to the development of the gyre. The results also suggest an impact from the jet in the strait on the coastal flow along the coast of Japan.

**Plain Language Summary**

The Tsugaru Warm Current forms part of the coastal flow around Japan and shows remarkable seasonal changes in its flow pattern, which are similar to the Kuroshio meandering. The current flows along the coast from winter to spring, but demonstrates large anticyclonic meandering in the offshore direction, known as "gyre mode", from summer to autumn. The cause of this change in the flow pattern has been thought to be the seasonal change in volume transport. In this study, we used high-resolution temporal and spatial data obtained from a high-frequency radar system, as well as the relationship between coastal waves and offshore jets with fronts, to identify another important factor that affects the seasonal flow pattern of the current, namely, "vorticity". Our results demonstrate the applicability and effectiveness of the high-frequency radar monitoring, and that it could be successfully used in other coastal regions, including other parts

43    of the same strait. Moreover, our study indicates that the response of the flow in the strait to

44    volume transport and vorticity will be important to long-term changes in the wider circulation in

45    relation to global warming and decadal-scale changes.

46

## 1 Introduction

47

48       The Tsugaru Strait is located between the mainland of Japan (Honshu) and Hokkaido

49 (Figure 1a). The Tsugaru Warm Current (TWC; Figure 1a) is a branch of the Tsushima Warm

50 Current, which itself has origins in the Kuroshio southwest of Kyushu island as well as the flow

51 from the Taiwan Strait (Isobe, 1999). The other branch flows north along the coast of Hokkaido

52 as the Soya Warm Current. These currents are closely related and can be considered one system

53 (e.g., Kida et al., 2016). In the Tsugaru Strait, a recent study (Wakita et al., submitted to GRL)

54 reported faster acidification than that in the global ocean. In addition, a far more intense vertical

55 mixing than in the open ocean, and enhancement of vertical nitrate transport above the

56 characteristic topography in the western part of the strait were also observed (Tanaka et al.,

57 2021). These recent studies suggest these characteristic phenomena that occur in the strait could

58 affect a wider region via the TWC.

59       The mean volume transport of the TWC and its seasonal variations have been estimated

60 as $1.5 \pm 0.3$ Sv, ($=10^6$ m$^3$ s$^{-1}$; e.g., Onishi and Ohtani, 1997; Nishida et al., 2003). Based on the

61 sea level difference between Fukaura and Hakodate (Figure 1b), Nishida et al. (2003) also

62 reported that the transport increases from spring to summer (maximum in July and August) and

63 decreases from autumn to winter (minimum in February). As another seasonal variation, there is

64 a remarkable change in the outflow pattern of the TWC from the eastern outlet of the strait. This

65 outflow switches from "coastal mode", which is a nearshore flow along the coast of the

66 Shimokita Peninsula (in winter and spring), to "gyre mode", which is a large anticyclonic gyre

67 that develops south of Hokkaido (in summer and autumn) (e.g., Conlon, 1982; Figure 1b). It is

68 thought that the increase in volume transport through the strait could initiate the development of

69 the gyre mode (e.g., Kawasaki and Sugimoto, 1988).

70    In addition to the volume transport, Kubokawa (1991; hereafter K91) raised another

71  important aspect of the difference in the vorticity across the jet based on the reduced gravity

72  model with vorticity-front (Figure S1). Using parameters such as the transport of water with a

73  relatively lower potential vorticity between the front and the boundary (area A in Figure S1), the

74  vorticity gap at the front, and the total volume transport at the outflow, K91 revealed that an

75  enhancement of the vorticity gap relative to the total volume transport is important for the

76  transition from "coastal" to "gyre" mode, in addition to an exceeding of the volume transport of

77  the lower potential vorticity fluid at the outlet of the strait relative to that at the far downstream

78  region. Although Nof and Pichevin (1999) proposed that the Tsugaru and the Alboran gyres

79  could develop regardless of the initial vorticity, and they also commented on the importance of

80  on-site estimation of vorticity in the currents as a subject for future investigation.

81    However, because of the lack of temporal and spatial observations from vessels and

82  moorings, the importance of the vorticity associated with the jet remains to be fully clarified.

83  This lack of observational data arises because it is difficult to estimate the mean geostrophic field

84  from time-limited shipboard current measurements, such as those made using acoustic Doppler

85  current profilers, because of the strong tidal current in the strait (Isoda and Baba, 1998; Onishi et

86  al., 2004; Luu et al., 2011; Ohta et al., 2014; Yamaguchi et al., 2020; Matsuura and Isoda, 2020).

87  The use of multiple moorings across the jet is also difficult due to the intense velocity and

88  frequent ship traffic through the strait. Moreover, although satellite observations can provide

89  gridded time series data covering a long period, the spatial resolution with respect to velocity is

90  too coarse for vorticity analysis.

91    Therefore, in this study, we used high-frequency radar (HFR) for surface current

92  monitoring in the eastern part of the strait (Figure 1c). This system can provide suitably high-

93  resolution spatial data, and also long-term and homogeneously (equally spaced in time)

94  continuous data that allowed us to estimate the background quasi-geostrophic current distribution

95  for the vorticity analysis. Using the data obtained by the HFR system developed by the Mutsu

96  Institute for Oceanography (MIO), Japan Agency for Marine-Earth Science and Technology

97  (JAMSTEC), we confirmed the effect of the vorticity gap at the jet axis based on the diagram

98  proposed by K91. Our results, which are in good agreement with the theory of K91, will be

99  presented below, after a brief explanation of our data analysis methods and the theory described

100  in K91. Moreover, the role of the eastern part of the strait will be discussed from the point of

101  view of the island circulation along the coast, which might be a contributor to the long-term

102  variations and/or rapid shifts in environmental conditions.

103

## 2 Materials and Methods

105  Surface velocity data for the eastern Tsugaru Strait were obtained from the MIO ocean

106  radar data site (MORSETS; https://www.godac.jamstec.go.jp/morsets/e/top/). The monitoring

107  system comprises three high-frequency radars (SeaSonde, 13.9 MHz, CODAR Ocean Sensors)

108  located in the Tsugaru Strait: two on the Shimokita Peninsula and the other on Hokkaido (Figure

109  1c). The system yields velocity distributions with a horizontal resolution of approximately 3 km

110  every 30 minutes, and the same system has also been used to monitor the Tsushima Warm

111  Current (e.g., Yoshikawa et al., 2006). We used data covering the period between March 2014,

112  when observations began, and December 2019. Data were collected from within the region

113  bounded by 140.93–141.98°E and 41.38–42.05°N (Figure 1c).

114     To investigate seasonal changes in the mean velocity field, we estimated the

115     climatological mean of zonal velocity, $U$, with respect to a series of 5-km zonal bands, which

116     were set from 140.92°E to 142.04°E with a half-overlap (Figure 1c). Within this zone, the

117     climatological mean was estimated each day from January 1st to December 31st over the period

118     2014–2019, using a width of 10 days. Outliers were excluded if they had a value that fell outside

119     of three standard deviations from the mean. Examples of the seasonal variation of $U$ are shown

120     in Figure 2a and b. The axis of the jet was defined as the latitude of the $U$-maximum (extremum).

121     In addition, the meridional distribution of $U$ was used to estimate the ratio of the vorticity gap at

122     the front to the total volume transport at the outflow through calculation of the difference in $U$

123     and its accumulation (integration) from the northern boundary of the grid, as described below.

124     Before that, the parts of K91 relevant to the present study will be briefly introduced.

125     Under conditions of stratification with a deep and passive lower layer, together with a

126     small Rossby number, $\varepsilon \ll 1$, and using the governing equations of the upper layer without

127     viscosity and diffusion, K91 set the geostrophic stream function with respect to the second order

128     term, $O(\varepsilon)$, along the north–south section at the outlet of the strait as follows.

129
$$\psi_{(\alpha)} = \begin{cases} 0 & \text{for } \alpha \leq -w \\ \frac{h_0 + P\{\cosh l - 1\}}{\sinh w} \sinh(\alpha + w) \\ h_0 & \text{for } \alpha \geq 0 \end{cases}$$

130
$$-\begin{cases} 0 & \text{for } -w < \alpha \leq -l, \\ P\{\cosh(\alpha + l) - 1\} & \text{for } -l < \alpha \leq 0, \end{cases} \quad (1)$$

131     Here, $\alpha$ denotes the north–south direction (southward positive), $\alpha = 0$ indicates the

132     southern edge of the strait (Figure S1), and $w$ is the width of the strait. In addition, $h_0$ represents

133     the total volume transport of the outflow, and $P$ represents the gap in vorticity at the front, that is,

134     with respect to the distribution of the potential vorticity, $q$, along the section at the outlet, which

135     we defined as (Figure S1):

136
$$q = \nabla^2 \psi - \psi = \begin{cases} -P & \text{for } -l \leq \alpha < 0, \\ 0 & \text{for } -w < \alpha < -l, \end{cases} \quad (2)$$

137     The ratio of the volume transport of the low potential vorticity fluid ($q = -P$, $P > 0$) to the

138     total volume transport $Q_R$ can be written as follows:

139
$$Q_R = 1 - \psi_{(-l)}/h_0, \quad (3)$$

140     On the other hand, K91 set the distribution of the stream function in the $\beta$ (west–east)

141     direction in the downstream region ($\alpha \to \infty$) as follows:

142     $\psi_{(\beta)} = \{h_0 + P(\cosh L - 1)\}e^{-\beta}$

143
$$- \begin{cases} P\{\cosh(L - \beta) - 1\} & \text{for } \beta < L, \\ 0 & \text{for } \beta \geq L, \end{cases} \quad (4)$$

144     where $L$ is the front location from the western boundary (Figure S1). The ratio of the

145     transport of the low potential vorticity fluid to the total transport there, $Q_{Rc}$, can be written as

146     follows:

147
$$Q_{Rc} = \begin{cases} 1 - P/2h_0 & \text{for } P/h_0 < 1, \\ h_0/2P & \text{for } P/h_0 \geq 1, \end{cases} \quad (5)$$

148     Then, following Stern (1986), K91 provided the condition regarding the propagating

149     direction of the long frontal wave using the parameters referred to above:

150     $c = \{h_0 - P(1 - e^{-L})\}e^{-L}, \quad (6)$

151     where, $c$ is the propagating speed of the long frontal wave. Thus, when $c$ is negative, the

152     wave propagates upstream. Using this condition, K91 defined three domains in the $P/h_0$–$Q_R$

153    plane as a diagnostic diagram for the flow pattern: (I) a steady coastal mode with $Q_R < Q_{Rc}$, (II) a

154    widening coastal mode with $Q_R > Q_{Rc}$ and $P/h_0 < 1$, and (III) a gyre mode with $Q_R > Q_{Rc}$ and

155    $P/h_0 \geq 1$. We applied this diagnostic diagram to the parameters estimated from the surface

156    velocity data obtained from MORSETS.

157          First, we estimated the ratio of the volume transport of the low potential vorticity fluid to

158    the total volume transport along the outlet of the strait, $Q_R$. We defined the accumulation of the

159    climatological mean of the zonal velocity from the northern boundary as $\psi$', assuming that $\psi$' at

160    the northern boundary was zero. The accumulations at the axis of the jet and the southern coastal

161    boundary or boundary of the HFR observation (Figure 1c) were defined as $\psi'_{(-l)}$ and $h_0$',

162    respectively. Then, equivalent $Q_R$' was defined as:

163    $$Q_R' = 1 - \psi'_{(-l)}/h_0', \quad (7)$$

164          Here, we assumed that $\psi'_{(-l)}/h_0$' was equivalent to $\psi_{(-l)}/h_0$ as defined by K91.

165          Second, we estimated the ratio of the gap in the vorticity at the front to the total volume

166    transport, $P'/h_0$', as follows. The difference in the zonal velocity, $\psi'_{\alpha\alpha}$, was calculated as the

167    representation of the second derivative of the geostrophic stream function. The locations of the

168    maximum and minimum of $\psi'_{\alpha\alpha}$ were defined as $\alpha_1$ and $\alpha_2$ (Figure 2c and d). When the multiple

169    maxima were obtained, especially in winter, we defined the location of the northern maximum as

170    $\alpha_1$ and the adjacent southern minimum as $\alpha_2$ (Figure 2d), because the southern coastal mode of

171    the TWC in winter has larger Rossby number (>0.4) than that of the northern coastal mode

172    (<0.4; T. Yasui, personal communication, 2021). Then, in the present study, the equivalent gap

173    in the vorticity at the front, $P$', was estimated using observed gap, $\psi'_{\alpha\alpha(\alpha 1)} - \psi'_{\alpha\alpha(\alpha 2)}$, as follows:

174    $$P' = \psi'_{(-l)} \times \left( \psi'_{\alpha\alpha(\alpha_1)} - \psi'_{\alpha\alpha(\alpha_2)} \right) / \psi'_{\alpha\alpha(\alpha_1)}, \quad (8)$$

175          Assuming that $P'/h_0' = P/h_0$, we used $P'/h_0'$ as another parameter in the diagnosis. Then,

176   the maximum value of the ratio of the volume transport of the low potential vorticity fluid to the

177   total volume transport in the far downstream region, $Q_{Rc}'$, was defined following K91.

178          Using the parameters $Q_R'$, $Q_{Rc}'$, and $P'/h_0'$, we investigated the flow pattern of TWC

179   based on the diagram suggested by K91. The index of the flow pattern (coastal or gyre) was

180   defined using the intensity of the meridional velocity at the outlet of the strait. The climatological

181   mean of the meridional velocity in each bin (Figure 1c), $V$ (northward positive), was calculated.

182   Then, the meridional average of the velocity over the area 41.51–41.67°N was calculated in each

183   bin located between 141.42°E and 141.63°E for each day as $\langle V \rangle_{41.51-41.67°N}$. Seasonal changes in

184   the meridional velocity at the outlet of the strait are shown in the Results and Figure 3. Then, the

185   zonal mean (141.42–141.63°E for $Q_R'$, $Q_{Rc}'$, and $P'/h_0'$, and 141.54–142.04°E for

186   $\langle V \rangle_{41.51-41.67°N}$) was calculated again to plot the parameters on the $Q_R–P/h_0$ plane, and we

187   diagnosed the flow pattern by comparing it with the meridional velocity at the outlet (Figure 4).

188

189   **3 Results**

190          The seasonal distribution of $U$ across the strait at 141.29–141.38°E (Region-a) and at

191   141.50–141.58°E (Region-b) are shown as examples in Figure 2a and b, respectively. Both

192   figures indicate a northward shift of the eastward jet, and an opposite westward flow to the south

193   of the jet in summer, implying the occurrence of an anticyclonic flow structure south of the jet.

194   In Region-b, $U$ shows a bimodal distribution, with a stronger coastal peak and the other a weaker

195   enhancement in the center of the strait (41.7–41.8°N, Figure 2b). Whereas the intensity of $U$

196   around the axis increased during summer in Region-a, in Region-b, $U$ near the coast increased

197     during winter (Figure 2b). In other words, our results suggest the disappearance of the near-coast

198     eastward current at the outlet in summer. This seasonal shift of the jet axis within the strait was

199     consistent with that reported by Abe et al. (2020).

200             The distribution of $\psi'_{\alpha\alpha}$ also showed a clear seasonal variation (Figure 2c and d)

201     associated with that of $U$. An increase in the vorticity gap across the front coincident with the

202     axis was recognized in summer. This was especially evident in Region-b, where the spring–

203     summer bimodal distribution was replaced by a well-defined single maximum to the north of the

204     jet axis, and a clear minimum near the southern boundary of the vorticity (Figure 2d).

205             Consequently, the large gap between the pair was estimated at the outlet of the strait as a

206     result of the enhanced single-peak jet having a spatial scale similar to that of the width of the

207     strait. On the other hand, $h_0'$ calculated as an accumulation of $U$ along the meridional direction,

208     also showed an increase in summer, especially in Region-a (Figure 2c). Thus, as a next step, we

209     calculated the ratio of $P'$ to $h_0'$ for each climatological day from January 1st to December 31st,

210     and compared its spatio-temporal plot with that of $Q_R'$.

211             The seasonal variation of $P'/h_0'$ showed clear intensification during the summer, reaching

212     a value of 2.5 (Figure 3a). This seasonal contrast in $P'/h_0'$ was especially remarkable in the

213     region above the Shiriya Spur (141.4–141.6°E, Figure S2). The maximum value of 2.5 occurred

214     in August in this region, and from June to November it was generally greater than 1. In contrast,

215     after November, $P'/h_0'$ decreased rapidly to less than 1. In addition to the high value of $P'/h_0'$

216     during summer, $Q_R'$ also showed a relatively large value (0.3–0.5) between June and November,

217     although $Q_R'$ temporarily became smaller than 0.3 in August when $P'/h_0'$ reached its maximum.

218     The meridional velocity in the region of the outlet showed the development of northward

219     velocity from June to the middle of August, and this continued until November (Figure 3b). The

220     peak date of $P'/h_0'$ corresponded with that of the northward velocity (mid-August). Thus, we

221     suggest that the gyre develops from June to mid-August under the high $P'/h_0'$ conditions. The

222     maintenance of the gyre is also implied until November under conditions of $P'/h_0' = 1.0–1.5$ and

223     $Q_R' = 0.3–0.5$, which is consistent with the findings of previous studies (e.g., Conlon, 1982;

224     Rosa et al., 2007). In the upstream region of 141.1–141.4°E, although $P'/h_0'$ generally exceeded

225     1 throughout year, $Q_R'$ remained below 0.3, except during summer, which implies that the

226     conditions required for gyre development were also established during the summer (Figure 3a).

227        Next, to compare the result obtained from our HFR observations with the theory

228     suggested by K91, we calculated the zonal mean of $P'/h_0'$ and $Q_R'$ over the region 141.42–

229     141.63°E, at just the outlet of the strait (Figures 3 and S2). After that, each parameter was plotted

230     on the diagnostic diagram proposed by K91 using a color scale to indicate the meridional

231     velocity at the outlet (Figure 4). The result was clearly consistent with K91; i.e., the dots located

232     in the gyre (coastal) mode region showed an intense northward (southward) current at the outlet

233     of the strait. Although an increase in $Q_R'$ to 0.3–0.5, together with a $P'/h_0'$ value of slightly less

234     than 1, were evident in spring (April–June), the current direction around the outlet of the strait

235     was towards the south, suggesting that the gyre does not develop under these conditions. In

236     contrast, although $Q_R'$ showed a constant value of approximately 0.3 during the summer (July–

237     September), the northward current around the outlet was indicated by the large value of $P'/h_0'$

238     (>1.5).

239

240    **4 Discussion**

241    Our results are consistent with the theory proposed by K91 (Figure 4). Therefore, the

242    importance of the vorticity gap at the front (the axis of the TWC) as a factor in gyre formation

243    (in addition to the volume transport of the TWC) has been confirmed again using our

244    observational data obtained from the HFR. With respect to the annual data, the distribution of

245    each parameter in the diagnostic diagram was similar to that of the six-year climatological data,

246    although there were exceptions. Consequently, we conclude that our results support the

247    reliability and effectiveness of using high-resolution HFR observations with the diagnostic

248    scheme, and also its applicability to other coastal regions such as the Alboran Sea. However,

249    note that the TWC shows large seasonal variability in stratification (e.g., Sugimoto and

250    Kawasaki, 1984), and this kind of diagnostic approach should be treated with caution, especially

251    in winter when the stratification is weaker.

252    To test our HFR approach, we also applied it to an upstream region of the same strait

253    (Figure S3). One of the notable characteristics of the seasonal changes in the flow within the

254    upper section of the strait during summer was the disappearance of the coastal eastward current

255    at the outlet and the northward shift of the flow, which had only a single axis (Figure 2b). This

256    caused the sharp single peak in the jet and the large vorticity gap at the front, which contributed

257    to the mode change. The cause of the disappearance and shift in the flow remains one of the

258    issues to be addressed. The application of the theory of outflow from the strait may be

259    reasonable, because the coastline of the peninsula extends southwards in the region east of

260    141.1 °E (Figure S3a). Thus, frontal wave stagnation there may occur as another sub-gyre in the

261    region. In fact, in summer, negative vorticity development related to the meridional velocity was

262    evident around 141.2–141.4°E (Figure S3b) in association with the high $P/h_0$ conditions in the

263    region 141–141.2°E (Figure S3c). Development of the sub-gyre could push the axis to the north,

264    and weaken the downstream flow along the northern coast. Note that this approach in this

265    upstream region should be treated with caution, again, because the Rossby number in this region

266    would be larger than that in the outlet of the strait. Thus, investigations of the sub-gyre

267    development are ongoing based on the coastal monitoring networks of MORSETS. Moreover,

268    the cause of seasonal change in the jet form should also be examined in relation to other physical

269    processes, including water mass distribution, tides, and volume transport by the TWC itself

270    (which would be related to wind stress curl).

271        The modulation of TWC such as the developments of the gyres during summer, suggests

272    that the Tsugaru Strait has an important impact on the system of the currents along the Japanese

273    coast including the Tsushima Warm Current, and the Kuroshio. Kida et al. (2020) explained that

274    the increasing trend seen in the volume transport of the Tsushima Warm Current reflects the

275    long-term northward (coastward) shift of the Kuroshio axis. This interpretation was based on the

276    assumption that the integration of the horizontal frictional torque caused by the coastal flow

277    around the islands (including Honshu, Kyushu, and Shikoku; Figure 1a) should be zero under

278    steady-state conditions (Yang, 2007; Kida et al., 2016). The development of the gyre and the

279    associated offshore movement of the flow path in the Tsugaru Strait may affect the integration of

280    the horizontal frictional torque caused by the coastal flow. Thus, it will be worthwhile

281    investigating the role of the Tsugaru Strait more carefully in relation to the increasing trend in

282    the volume transport in the upstream region.

283        Moreover, the decadal variability of the circulation within the upstream region may cause

284    similar variations in the TWC. Kaneko et al. (2018) reported a shift in the Kuroshio axis along

285    141°N, which was synchronous with both a stable Kuroshio Extension and the Pacific Decadal

286 Oscillation, and this situation persisted for about 10 years after the 1998/1999 regime shift. If

287 such a synchronized shift of the axis could cause changes in the transport of the TWC, rapid

288 changes in biota synchronized with the shift might be caused along the warm currents around

289 Japan, including the TWC. Recently, the northward expansion of harmful dinoflagellates into the

290 strait, which can cause red tides, was reported, and transport by the TWC was suspected as one

291 of causes (Shimada et al., 2016). Therefore, in future, the role of the eastern part of the Tsugaru

292 Strait in the modulation of the flows should be clarified with respect to both long-term trends and

293 decadal variations, as this could have a large impact on the biota. Enlargement of HFR

294 observations, development of high-resolution numerical models, and enhancing the coastal

295 observation networks, including monitoring buoys, would all contribute to this task.

296

304

## References

306 Abe, H., K. Sasaki, T. Yasui, and M. Wakita (2020) Observation of Tsugaru warm current by
307 High Frequency Radar and preliminary result for its prediction, *Kaiyo Monthly*, 52, 312–316. (in
308 Japanese)

309 Conlon, D. M. (1982), On the outflow modes of the Tsugaru Warm Current, *La mer*, 20, 60–64.

310 Isobe, A. (1999) On the origin of the Tsushima Warm Current and its seasonality. *Cont. Shelf*
311 *Res.*, 19 (1), 117–133. https://doi.org/10.1016/S0278-4343(98)00065-X

312 Isoda, Y., and K. Baba (1998), Tides and tidal currents in the Tsugaru strait. *Bull. Fac. Fish.*
313 *Hokkaido Univ.*, 49 (3), 117– 130 (in Japanese with English abstract)

314 Japan Agency for Marine-Earth Science and Technology MORSETS website (2020), MIO ocean
315 radar data site for Eastern Tsugaru Strait. https://www.godac.jamstec.go.jp/morsets/e/top/.
316 Accessed on 22 Nov. 2020

Kaneko, T. Okunishi, T. Seto, H. Kuroda, S. Itoh, S. Kouketsu, and D. Hasegawa (2018), Dual effects of reversed winter–spring temperatures on year-to-year variation in the recruitment of chub mackerel (*Scomber japonicus*), *Fish. Oceanogr.*, 28, 1–16, https://doi.org/10.1111/fog.12403

Kawasaki, Y. and T. Sugimoto (1988), A laboratory study of the short-term variation of the outflow pattern of the Tsugaru Warm Water with a change in its volume transport. *Bull. Tohoku Reg. Fish. Res. Lab.*, 50, 203–215 (in Japanese with English abstract)

Kida, S., B. Qi, J. Yang, and X. Lin (2016) The annual cycle of the Japan Sea Throughflow. *J. Phys. Oceanogr.*, 46 (1), 23–39, doi: 10.1175/JPO-D-15-0075.1

Kida, S., K. Takayama, Y. N. Sasaki, H. Matsuura, and N. Hirose (2020), Increasing trend in Japan Sea Throughflow transport, *J. Oceanogr.*, https://doi.org/10.1007/s10872-020-00563-5

Kubokawa, A. (1991), On the behavior of outflows with low potential vorticity from a sea strait. *Tellus A*, 43, 168–176. https://doi.org/10.1034/j.1600-0870.1991.t01-1-00007.x

Luu, Q. H., K. Ito, Y. Ishikawa, and T. Awaji (2011), Tidal transport through the Tsugaru Strait — part I: Characteristics of the major tidal flow and its residual current. *Ocean Sci. J.*, 46, 273–288. https://doi.org/10.1007/s12601-011-0021-z

Matsuura, H., and Y. Isoda (2020), Pseudo-fortnightly variation produced by interaction between passage-flow and diurnal tidal currents in the Tsugaru Strait, *Bull. Fac. Fish. Hokkaido Univ.*, 70 (1), 13–23, doi:10.14943/bull.fish.70.1.13

Nishida, Y., I. Kanomata, I. Tanaka, S. Sato, S. Takahashi, and H. Matsubara (2003), Seasonal and Interannual Variations of the Volume transport through the Tsugaru Strait. *Oceanogr. Jpn*, 12 (5), 487–499, https://doi.org/10.5928/kaiyou.12.487 (in Japanese with English abstract)

Nof, D., and T. Pichevin (1999) The Establishment of the Tsugaru and the Alboran Gyres. *J. Phis. Oceanogr.*, 29(1), 39–54, DOI: https://doi.org/10.1175/1520-0485(1999)029<0039:TEOTTA>2.0.CO;2

Onishi, M., and K. Ohtani (1997) Volume transport of the Tsushima Warm Current, west of Tsugaru Strait bifurcation area. *J. Oceanogr.*, 53(1), 27–34,

Onishi M., Y. Isoda, H. Kuroda, M. Iwahashi, C. Saitoh, T. Nakayama, T. Ito, K. Iseda, K. Nishizawa, S. Shima, and O. Togawa (2004), Winter Transport and Tidal Current in the Tsugaru Strait. *Bull. Fac. Fish. Hokkaido Univ.*, 55 (2), 105–119.

Ohta, S., Y. Isoda, S. Yoshimura, K, Syouji, S. Arita, K. Kawano, X. Fang, and N. Kobayashi (2014), Internal tidal waves generated over the sill topography in the Tsugaru Strait, *Sea and Sky*, 90 (5), 63–84, (in Japanese with English abstract)

Rosa, A. L., Y. Isoda, K. Uehara, and T. Aiki (2007), Seasonal Variations of Water System Distribution and Flow Patterns in the Southern Sea Area of Hokkaido, Japan. *J. Oceanogr.*, 63, 573–588, doi:10.1007/s10872-007-0051-4.

Shimada, H., M. Kanamori, H. Yoshida, and I. Imai (2016), First record of red tide due to the harmful dinoflagellate *Karenia mikimotoi* in Hakodate Bay, southern Hokkaido, in autumn, 2015. *Nippon Suisan Gakk.*, 82(6), 934–938, https://doi.org/10.2331/suisan.16-00033, (in Japanese with English abstract)

357 Stern, M. E. (1986), On the amplification of convergences in coastal currents and the formation
358 of "squirts". *J. Mar. Res.*, 44 (3), 403–421, https://doi.org/10.1357/002224086788403097

359 Sugimoto, T., and Y. Kawasakai (1984) Seasonal and year-to- year variations of the Tsugaru
360 Warm Current and their dynamical interpretation. *Bull. Coastal Oceanogr.*, 22, 1–11 (in
361 Japanese).

362 Tanaka, T, H. Hasegawa, T. Okunishi, H. Kaneko, and T. Ono (2021), Internal Hydraulic Jump
363 in the Tsugaru Strait, *J. Oceanogr.* https://doi.org/10.1007/s10872-020-00588-w

364 Yamaguchi, T., Y. Isoda, U. Itoh, T. Mukai, and N. Kobayashi (2020), Observation and model
365 experiments on an internal-wave packet accompanied by streak bands over the sill topography of
366 Tsugaru Strait, *Oceanogr. Jpn,* 29 (3), 71–90, https://doi.org/10.5928/kaiyou.29.3_71 (in
367 Japanese with English abstract)

368 Yang, J. (2007), An oceanic current against the wind: how does Taiwan Island steer warm water
369 into the East China Sea? *J. Phys. Oceanogr.*, 37 (10) 2563–2569, doi: 10.1175/JPO3134.1

370 Yoshikawa, Y., A. Masuda, K. Marubayashi, M. Ishibashi, and A. Okuno (2006), On the
371 accuracy of HF radar measurement in the Tsushima Strait, *J. Geophys. Res.*, 111, C04009,
372 doi:10.1029/2005JC003232.

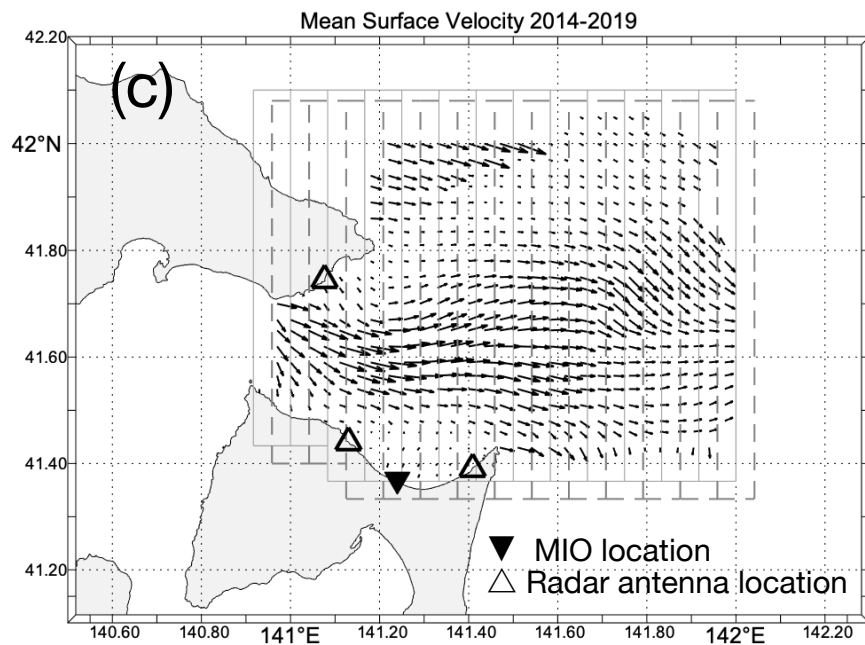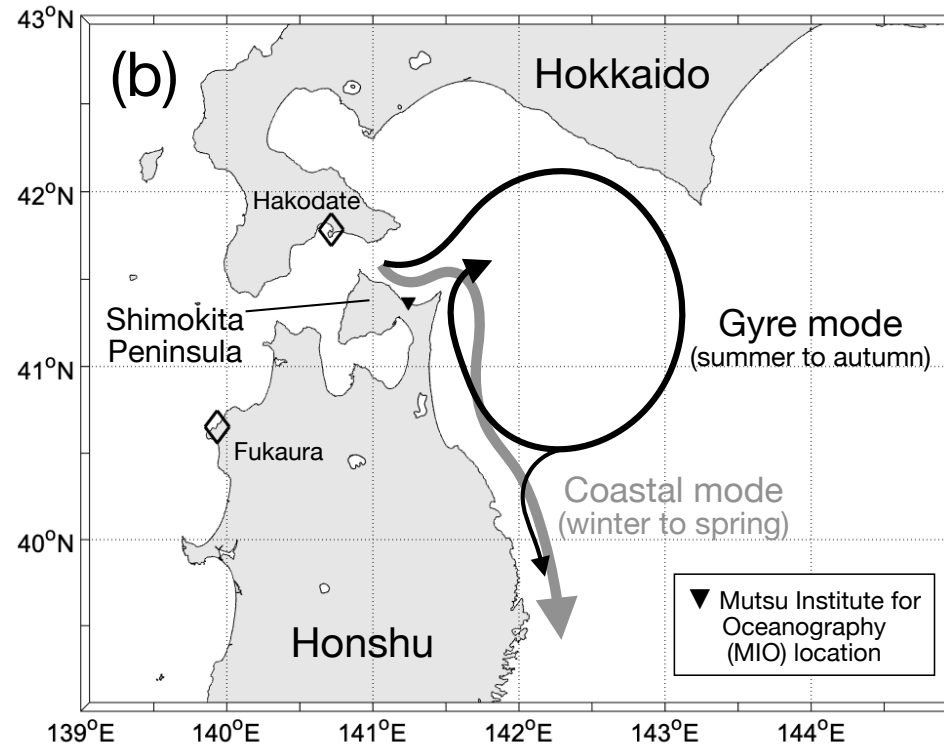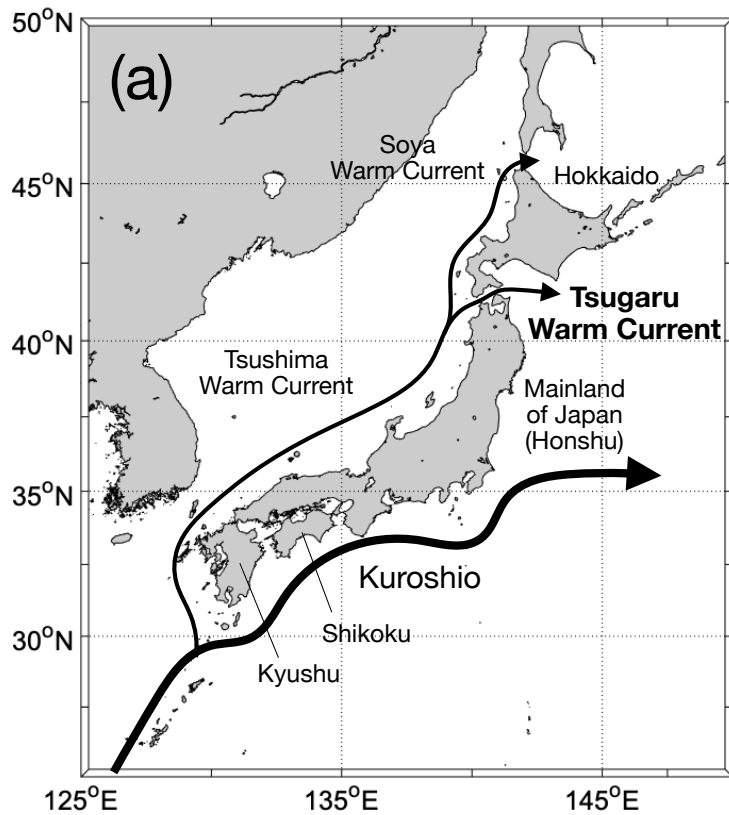373

374

375 **Figure captions**

376 **Figure 1**. (a) Schematic diagram of the flows around Japan. (b) Seasonal flow pattern of the
377 Tsugaru Warm Current. (c) Observation site of the present study and distribution of the temporal
378 mean velocity at each grid point. The square grids in (c) indicate the bins used to calculate the
379 zonal average of the zonal velocity.

380 **Figure 2**. Examples of date–latitude plots of (a) and (b) zonal velocity, and (c) and (d) $\psi'$ (thin
381 lines) and $\psi'_{\alpha\alpha}$ (color and thick lines). The left (right) column denotes Region-a (Region-b). The
382 black line in (a) and (b) denotes the latitude of the jet axis. The orange (blue) line in (c) and (d)
383 denotes the latitude of the maximum (minimum) of $\psi'_{\alpha\alpha}$. See text for definitions of $\psi'$ and $\psi'_{\alpha\alpha}$.

384 **Figure 3**. Longitude–date plot of (a) $Q_R'$ (color) and $P'/h_0'$ (contours), and (b) meridional
385 velocity averaged in north–south band. See text for definitions of $Q_R'$, $P'$, and $h_0'$.

386 **Figure 4**. The diagnostic diagram for the flow pattern.
387

**Figure 1.** (a) Schematic diagram of the flows around Japan. (b) Seasonal flow pattern of the Tsugaru Warm Current. (c) Observation site of the present study and distribution of the temporal mean velocity at each grid point. The square grids in (c) indicate the bins used to calculate the zonal average of the zonal velocity.
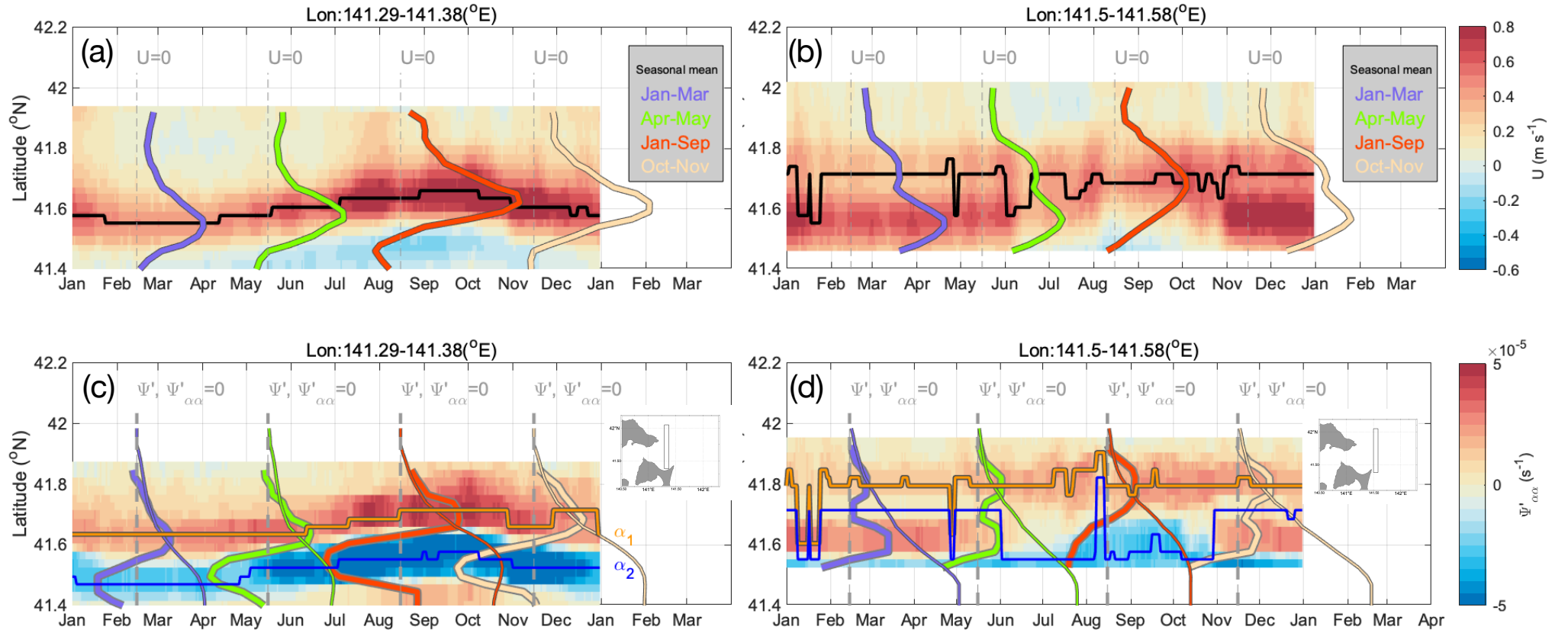
**Figure 2.** Examples of date–latitude plots of (a) and (b) zonal velocity, and (c) and (d) $\psi'$ (thin lines) and $\psi_{\alpha\alpha}'$ (color and thick lines). The left (right) column denotes Region-a (Region-b). The black line in (a) and (b) denotes the latitude of the jet axis. The orange (blue) line in (c) and (d) denotes the latitude of the maximum (minimum) of $\psi_{\alpha\alpha}'$. See text for definitions of $\psi'$ and $\psi_{\alpha\alpha}'$.
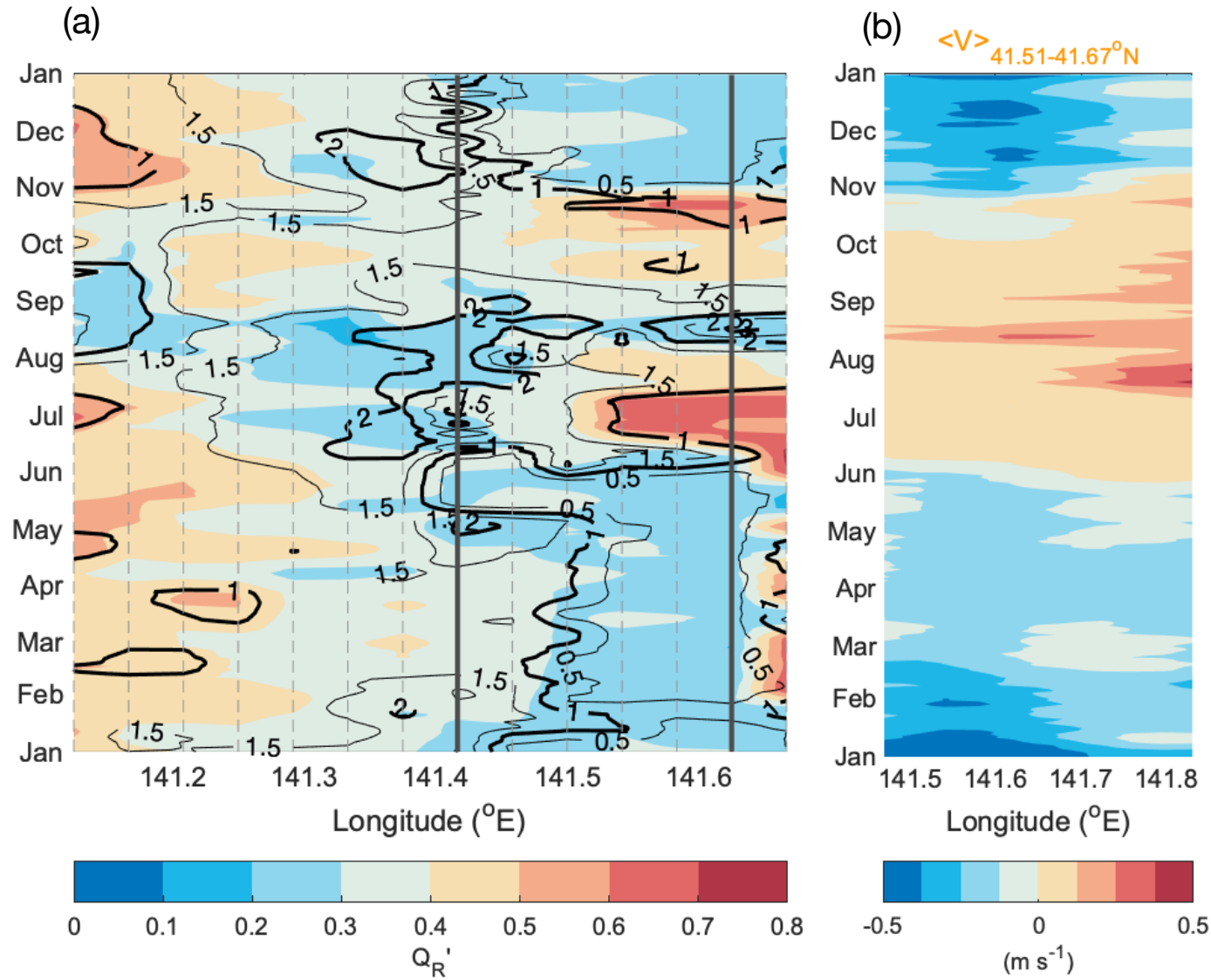
**Figure 3.** Longitude–date plot of (a) $Q_R'$ (color) and $P'/h0'$ (contours), and (b) meridional velocity averaged in north–south band. See text for definitions of $Q_R'$, $P'$, and $h_0'$.
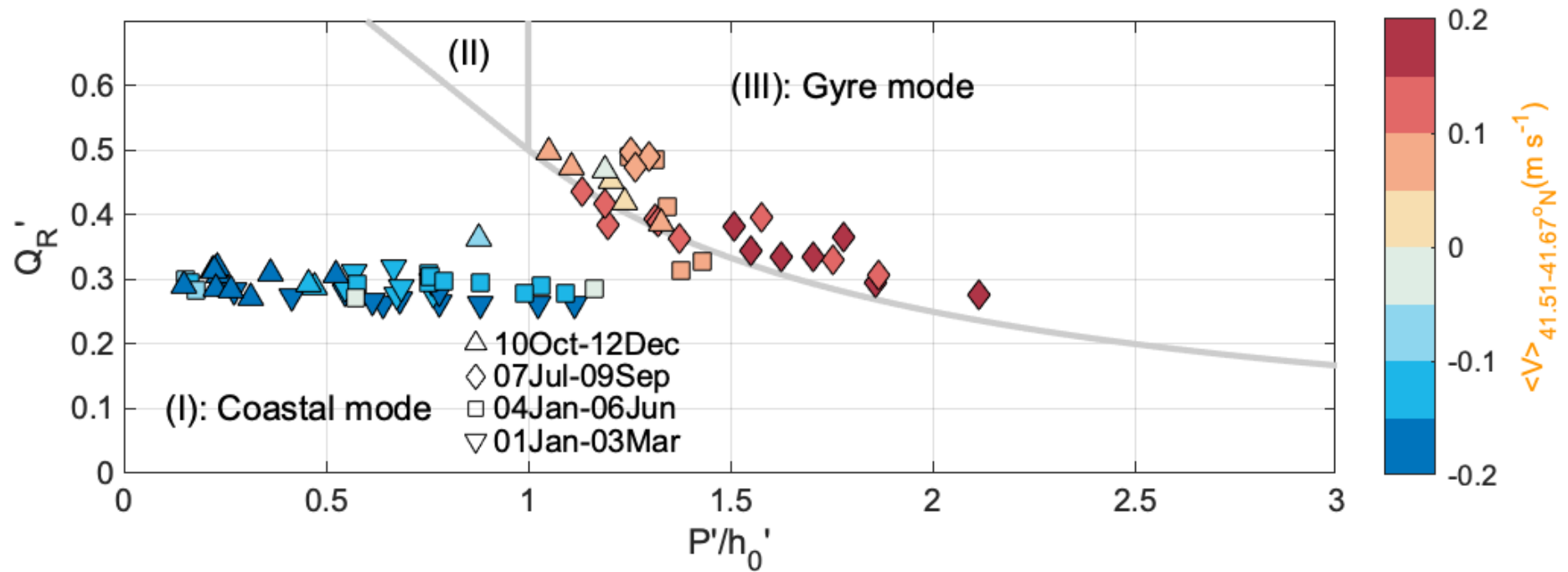
**Figure 4**. A diagnosis diagram of the flow pattern.